Antiferromagnetic spin structure and negative thermal expansion of $Li_2Ni(WO_4)_2$

Sunil K. Karna,[1] C. W. Wang,[2] R. Sankar,[1] M. Avdeev,[3] A. Singh,[4] I. Panneer Muthuselvam,[1] V. N. Singh,[5,6] G. Y. Guo,[6] and F. C. Chou[1,7,8,*]

[1]*Center for Condensed Matter Sciences, National Taiwan University, Taipei 10617, Taiwan, Republic of China*
[2]*Neutron Group, National Synchrotron Radiation Research Center, Hsinchu 30076, Taiwan, Republic of China*
[3]*Bragg Institute, ANSTO, Australia*
[4]*Harish-Chandra Research Institute, Allahabad 211019, India*
[5]*Institute of Atomic and Molecular Sciences, Academia Sinica, Taipei 10617, Taiwan, Republic of China*
[6]*Department of Physics, National Taiwan University, Taipei 10617, Taiwan, Republic of China*
[7]*National Synchrotron Radiation Research Center, Hsinchu 30076, Taiwan, Republic of China*
[8]*Taiwan Consortium of Emergent Crystalline Materials, Ministry of Science and Technology, Taipei 10622, Taiwan, Republic of China*

(Received 4 April 2015; revised manuscript received 17 June 2015; published 10 July 2015)

We report the results of a study on the crystal and magnetic structure of $Li_2Ni(WO_4)_2$ with a neutron diffraction technique. The Ni^{2+} spins of $S = 1$ for NiO_6 octahedra are coupled via corner-sharing, nonmagnetic double tungstate groups in a super-superexchange route. Two magnetic anomalies at $T_{N1} \sim 18$ K and $T_{N2} \sim 13$ K are revealed from the measured magnetic susceptibility $\chi(T)$, and T_{N2} is confirmed to be the onset of a commensurate long-range antiferromagnetic (AF) ordering through neutron diffraction. A negative thermal expansion phenomenon is observed below T_{N2}, which has been interpreted as a result of competing normal thermal contraction and long-range AF spin ordering through counterbalanced WO_4 and NiO_6 polyhedral local distortion. The AF spin structure has been modeled and used to show that Ni spins with a saturated magnetic moment of $\sim 1.90(27)\mu_B$ that lies in the a-c plane approximately $46^\circ(\pm 10^\circ)$ off the a axis. The experimental results are compared and found to be consistent with theoretical calculations using density-functional theory with a generalized gradient approximation plus on-site Coulomb interaction.

DOI: 10.1103/PhysRevB.92.014413 PACS number(s): 75.30.Et, 75.25.−j, 65.40.De

I. INTRODUCTION

The compounds of double tungstate have been given much attention in the past few decades because of their interesting magnetic properties, such as strong magnetic anisotropy, strong spin-lattice coupling, and magnetic low-dimensionalities [1]. The crystal structures, crystal chemistry, and phase diagrams of the double tungstate of Group IA and rare-earth elements have been reported to exhibit rich structural variations [2], mostly related to the additional degree of freedom of the flexible local distortion of tungstate polyhedra. In addition, they also show great potential in solid-state laser applications, nonlinear optic applications, and photocatalysts [3,4]. The transition-metal double tungstate $Li_2Ni(WO_4)_2$ was first synthesized and reported by Alvarez-Vega *et al.* [5]. A Raman scattering study and photocatalytic properties of $Li_2Ni(WO_4)_2$ have also been reported [4,6]. Recently, the physical properties of the $Li_2(Co,Cu)(WO_4)_2$ series have also been characterized in detail [7,8]. For $Li_2Co(WO_4)_2$ of $S = \frac{3}{2}$, which is isostructural to $Li_2Ni(WO_4)_2$ of $S = 1$, a unique two-step antiferromagnetic (AF) transition resulting from the consecutive triangular symmetry breaking within two near-orthogonal crystal planes under triclinic crystal symmetry has been found and interpreted, and the Co^{2+} spins have been shown to be coupled via a super-superexchange (SSE) route across the bridging double tungstate group. Facing the possibility of a Haldane chain spin gap opening for $Li_2Ni(WO_4)_2$ of $S = 1$, and a similar triclinic crystal structure of pseudotriangular symmetry in three respective crystal planes, it is desirable to explore the magnetic and crystal structure of $Li_2Ni(WO_4)_2$ compared with that of $Li_2Co(WO_4)_2$ [7].

In this work, we report the results of a neutron diffraction study on the low-temperature crystal structure and magnetic structure of $Li_2Ni(WO_4)_2$. Following the observation of the two magnetic anomalies revealed at $T_{N1} \sim 18$ K and $T_{N2} \sim 13$ K based on the homogeneous magnetic susceptibility $\chi(T)$, antiferromagnetic long-range spin ordering below $T_{N2} \sim 13$ K has been confirmed with neutron diffraction. Interestingly, a negative thermal expansion phenomenon below T_{N2} is revealed from the neutron diffraction structure analysis. Negative thermal expansion (NTE) is a phenomenon whereby a lattice expands upon cooling, which is anomalous and occurs in very few compounds discussed in the literature [9]. We tentatively explain the NTE phenomenon through the counterdistortion of double WO_4 and NiO_6 polyhedra, which is used to counter the normal thermal contraction by keeping the optimal interspin distance of AF long-range ordering (LRO) intact via spin-phonon coupling. The proposed AF spin structure using neutron diffraction data is compared and found to be consistent with that obtained from density-functional-theory (DFT) calculations.

II. EXPERIMENTAL DETAILS

A polycrystalline sample of $Li_2Ni(WO_4)_2$ was synthesized using a solid-state reaction technique. Stoichiometric quantities of high-purity (>99.95%) powders of NiO, Li_2CO_3, and WO_3 were mixed and heated at 550 and 650 °C for 24 h with intermittent grinding and pelletizing. Final annealing was performed at 700 °C for 160 h and followed by furnace cooling to room temperature at a rate of approximately 150 °C/h.

*Corresponding author: fcchou@ntu.edu.tw

The resultant compounds were yellow in color. X-ray and neutron powder diffractions were used to determine the crystal structure of the sample. The x-ray diffraction measurements were performed on a Bruker D8 ADVANCE diffractometer employing Cu $K\alpha$ radiation. The neutron diffraction measurements were conducted at the Bragg Institute, ANSTO, using the high-resolution powder diffractometer Echidna [$\lambda = 1.6215$ Å defined by Ge (335) crystals] for the crystalline structure analysis, and the high-intensity powder diffractometer Wombat [$\lambda = 2.9502$ Å defined by Ge (115) crystals with 120° take-off angle] for the magnetic structure analysis. To achieve a good signal-to-noise ratio, each diffraction pattern was collected for 4 h with an angular step of 0.05° using approximately four grams of sample loaded in a cylindrical vanadium can 6 mm in diameter. The sample temperature was controlled using a He-gas closed-cycle refrigeration (CCR) system. The magnetic measurements were performed using a SQUID magnetometer (Quantum Design, USA), employing standard setups.

III. RESULTS AND DISCUSSION

A. Crystalline structure

The high-resolution neutron diffraction patterns were analyzed using the General Structure Analysis System (GSAS) program following the Rietveld profile refinement method [10,11]. The refinements were performed assuming a triclinic symmetry with a space group of $P\bar{1}$. Figure 1 displays the observed (circles) and calculated (solid lines) diffraction patterns taken at 300 K, with differences plotted at the bottom, which indicates a satisfactory fitting according to the acceptable fitting indicator values of $R_p = 3.42\%$, $R_{wp} = 4.58\%$, and $\chi^2 = 3.154$. There are no identifiable traces of impurity phases present in the neutron diffraction patterns. The crystalline structure of $Li_2Ni(WO_4)_2$ can be viewed as a 3D arrangement of isolated NiO_6 octahedra that

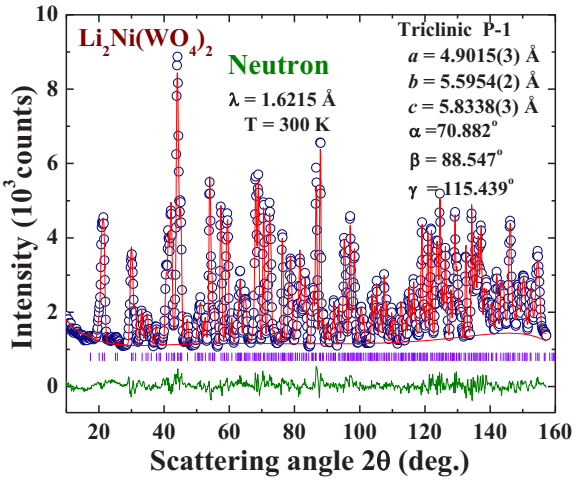

FIG. 1. (Color online) Observed (circles) and fitted (solid lines) high-resolution neutron powder diffraction patterns of bulk $Li_2Ni(WO_4)_2$ at 300 K, assuming a triclinic structure with space group $P\bar{1}$. The differences between the calculated and observed patterns are plotted at the bottom. The solid vertical lines mark the calculated positions of the Bragg reflections of the proposed crystalline structure.

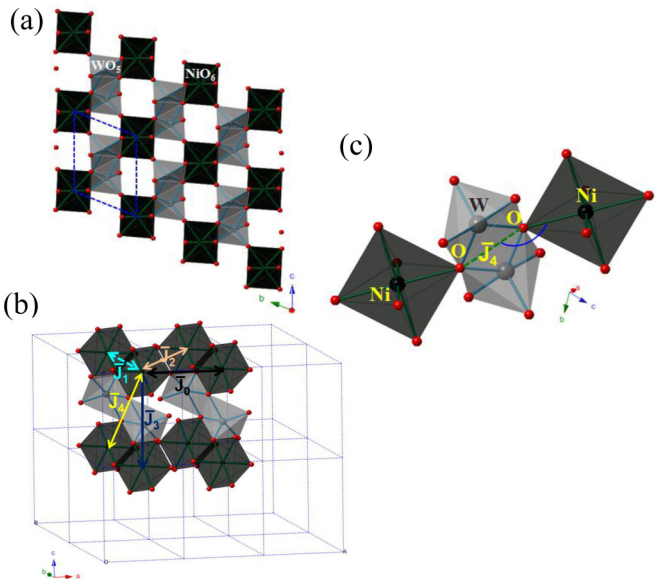

FIG. 2. (Color online) (a) The crystal structure of $Li_2Ni(WO_4)_2$ with triclinic symmetry in a projection view of the bc plane and Li atoms omitted for clarity. (b) The effective magnetic couplings along the three crystallographic axes ($\bar{J}_0$, $\bar{J}_1$, and $\bar{J}_3$) and the shorter diagonal ($\bar{J}_2$ and $\bar{J}_4$) directions within ab and bc planes of a triclinic crystal structure, which are qualitative and average descriptors different from the nearest-neighbor exchange interaction parameters of J_i described in Table III. (c) A schematic plot to illustrate the defined Ni-O $\cdots$ O bond angle for Ni-Ni spin coupling through the Ni-O-W-O-Ni super-superexchange route along the bc-diagonal direction ($\bar{J}_4$).

are corner-shared with the double WO_4 group, and the double WO_4 group is deformed into an edge-shared inverted square pyramid WO_5 pair (Fig. 2). The simplest view of $Li_2Ni(WO_4)_2$ is that the isolated NiO_6 octahedra are bridged by a double WO_4 group in three dimensions, and the Li atoms sit in the interstitial site due to their ionic nature. The magnetic couplings among Ni spins are expected to be established via super-superexchange Ni-O-W-O-Ni routes, as suggested by the effective magnetic couplings along the crystallographic axes ($\bar{J}_0$, $\bar{J}_1$, and $\bar{J}_3$) and diagonal ($\bar{J}_2$ and $\bar{J}_4$) directions indicated in Fig. 2.

B. Magnetic susceptibility measurement

Magnetic susceptibilities measured at applied field $H_a = 100$ Oe are shown in Fig. 3. There are two step drops found in $\chi(T)$ near ~18 and 13 K, as also clearly identified by the corresponding $d\chi/dT$ peaks in the inset. The Curie-Weiss law fitting using $1/\chi$ at high temperature (not shown) gives $\theta_{CW} = -27.5$ K and a Curie constant of 1.17(2) cm^3 K/mol corresponding to an effective moment of $\mu_{eff} = 3.06\mu_B$/Ni, which suggests the antiferromagnetic (AF) nature of the spin interaction. The effective moment $\mu_{eff} = 3.06\ \mu_B$/Ni is slightly larger than the theoretical spin-only ($S = 1$) value of $2.83\mu_B$ for Ni^{2+} due to the orbital contribution [12]. The two consecutive AF-like phase transitions of $Li_2Ni(WO_4)_2$ are defined as $T_{N1} = 18$ K and $T_{N2} = 13$ K. A similar two-step transition has also been observed in the isostructural compound $Li_2Co(WO_4)_2$ [7], where the two-step AF transition has been

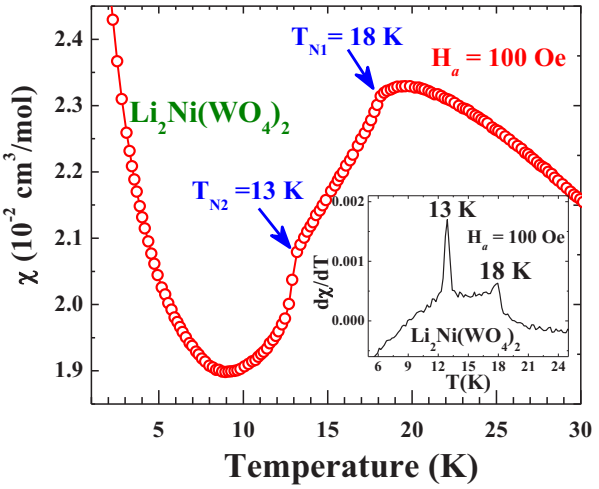

FIG. 3. (Color online) Temperature dependence of magnetic susceptibilities for $Li_2Ni(WO_4)_2$ measured at applied field of $H_a = 100$ Oe. The inset shows $d\chi/dT$ vs T.

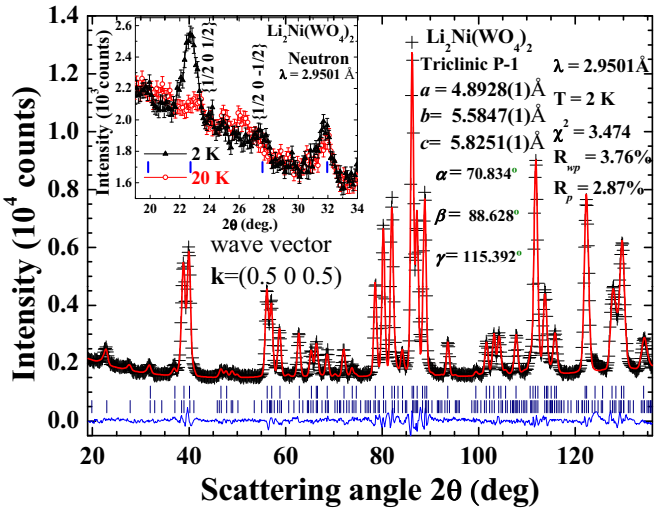

FIG. 4. (Color online) Observed (crosses) and fitted (solid lines) neutron powder-diffraction patterns taken at 2 K, assuming a triclinic $P\bar{1}$ symmetry for both the crystalline and magnetic structures. The differences between the calculated and observed patterns are plotted at the bottom. The two sets of solid vertical lines mark the calculated positions of the Bragg reflections of the proposed crystalline and magnetic structures. The inset shows the amplified view of the superlattice peak that appears below $T_{N2} \sim 13$ K and is indexed as $(\frac{1}{2}\ 0\ \frac{1}{2})$ in the $P\bar{1}$ space group.

tentatively assigned due to the consecutive symmetry breaking of the competing triangular Co sublattices within two near-orthogonal crystal planes of a triclinic crystal structure. Both transitions show a $\chi(T)$ step drop to indicate AF long-range ordering, and their 3D long-range ordering nature has also been confirmed by the observed specific heat C_p (T_N) cusps for $Li_2Co(WO_4)_2$.

C. Powder neutron diffraction study of magnetic structure

To elucidate the nature of the magnetic phase transitions, we have performed a high-intensity neutron powder diffraction study at low temperatures. Figure 4 shows the observed (crosses) and calculated (solid lines) neutron diffraction patterns at 2 K, assuming the $P\bar{1}$ symmetry for both the crystalline and Ni spins, with their differences plotted at the bottom. Neutron powder diffraction patterns were collected from 2 K in steps of 2 K during warming, as shown in Fig. 5. In addition to the room-temperature diffraction pattern that is indexed with the $P\bar{1}$ space group (Fig. 1), superlattice peaks emerge at 2 K, as shown in the inset of Fig. 4 for data in the low-Q regime, which can be easily indexed using the k-search program of the FULLPROF suite [13]. A commensurate magnetic propagation vector $\mathbf{k} = (\frac{1}{2}\ 0\ \frac{1}{2})$ is obtained, which strongly suggests a magnetic unit cell that is twice the size of the crystalline unit cell along both the a and c directions. By tracing both the diffraction pattern that is indexed with the $P\bar{1}$ space group and the superlattice peaks from 2 K during warming, an intensity contour mapping is obtained and shown in Fig. 5. It is clear that the superlattice $(\frac{1}{2}\ 0\ \frac{1}{2})$ peak disappears above $T_{N2} \sim 13$ K, which strongly suggests that the superlattice peak originates from the AF magnetic spin ordering, instead of due to other unknown structure change and before confirmation by the spin-polarized neutron diffraction experiment. The current neutron diffraction data failed to identify additional superlattice peaks that may correspond to the magnetic phase transition below T_{N1} and above T_{N2}, which could be due to the low intensity of superlattice peaks buried in the background or beyond the scanned Q-range. We believe that by analogy with $Li_2Co(WO_4)_2$ [14], an incommensurate LRO phase may be expected to exist in the $T_{N2} < T < T_{N1}$ range.

D. Proposed magnetic structure from neutron diffraction

One Ni atom per crystalline unit cell and three components per spin (m_a, m_b, and m_c) are needed to model the magnetic structure of $Li_2Ni(WO_4)_2$. By using the neutron diffraction data at 2 K in a magnetic spin structure fitting using the FULLPROF program [13], the unconstrained fitted

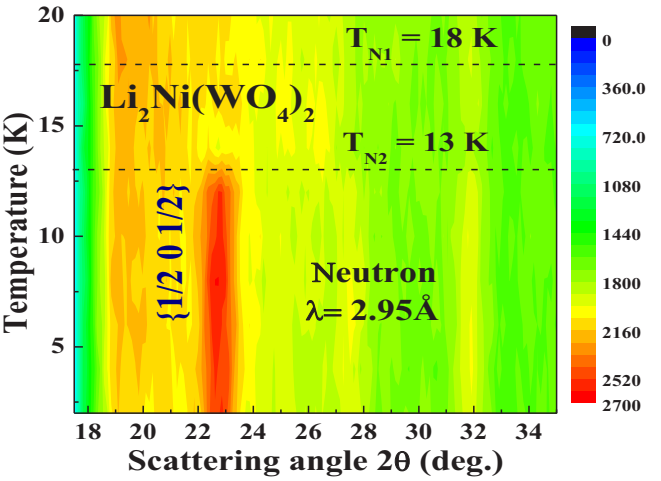

FIG. 5. (Color online) Temperature-scattering angle contour map of the $(\frac{1}{2}\ 0\ \frac{1}{2})$ superlattice peak at low temperature near T_{N1} and T_{N2}.

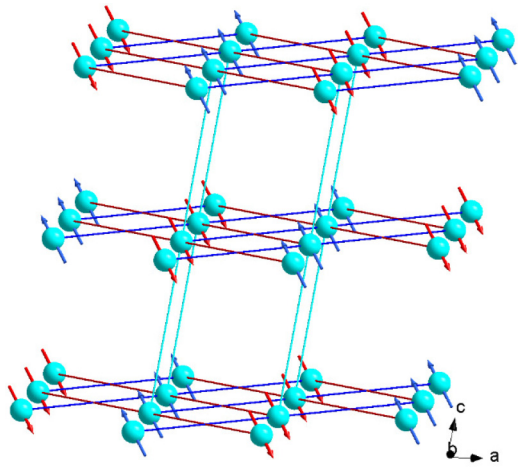

FIG. 6. (Color online) A schematic AF spin structure of $Li_2Ni(WO_4)_2$ based on the fitting of neutron diffraction data.

magnetic moment is [$m_a = 1.30(20)$, $m_b = -0.18(15)$, and $m_c = 1.29(20)$], where a large uncertainty for m_b indicates that the magnetic moments mainly lie in the a-c plane. With the constraint of $m_b = 0$ on refinement, $m_a = 1.32(20)\mu_B$ and $m_c = 1.40(18)\mu_B$ are obtained, resulting a magnetic moment of $1.90(27)\mu_B$ per Ni. The proposed magnetic structure is shown in Fig. 6, where the ferromagnetic chains along the b axis order antiferromagnetically along the a and c directions, and the spin direction is approximately $46^\circ(\pm 10^\circ)$ off the a axis.

Because all NiO_6 octahedra are corner-shared with the double WO_4 group in three dimensions, Ni spin couplings follow a super-superexchange (SSE) interaction route, instead of the common superexchange route for the regular oxide materials. Based on the geometric parameters associated with the super-superexchange Ni-O-W-O-Ni paths, we have considered five effective couplings along the major axes and diagonal directions, $\bar{J}_0$, $\bar{J}_1$, $\bar{J}_2$, $\bar{J}_3$, and $\bar{J}_4$, as shown in Fig. 2(b), which are tabulated in Table I with the corresponding interatomic distances and bond angles. According to the Goodenough-Kanamori (GK) phenomenological model for spin superexchange coupling, the shortest interspin distance at 180° is expected to have the strongest AF coupling but ferromagnetic (FM) coupling for closer to 90° [15,16]. On the other hand, Koo *et al.* proposed that the GK phenomenological rule does not apply to spin couplings via the SSE mechanism. [17] Instead, the oxygen-oxygen distance within the bridging polyhedron (O···O) dominates the strength of the spin coupling via the SSE route, especially when the O···O distance is shorter than the van der Waals distance (∼2.8 Å) [17]. Based on the bond length and bond angle analysis of the neutron diffraction data collected near T_{N2}, as shown in Table I, it is expected that $\bar{J}_1$ will show effective FM coupling because of the bond angle (∼102°) being close to 90°, and the O···O distance of 2.932 Å is significantly longer than the defined van der Waals distance; all other effective couplings show AF coupling for large bond angles closer to 180°. The current phenomenological analysis is consistent with the spin structure solved with neutron diffraction shown in Fig. 6. Interestingly, although the $\bar{J}_4$ along the shorter diagonal direction of the bc plane has the longest Ni-Ni distance (∼6.6 Å), implying the weakest AF coupling among these four, it corresponds to the shortest O···O distance (∼2.45 Å) and is expected to have the strongest AF spin coupling following the phenomenological SSE spin coupling rule.

E. Theoretical calculations of the magnetic structure

Theoretical calculations have been performed based on first-principles density-functional theory (DFT) with the generalized gradient approximation (GGA) [18]. To describe the electron-electron correlation associated with the 3d states of Ni, the GGA plus on-site Coulomb repulsion (GGA + U) [19] calculations are performed with an effective $U_{\text{eff}} = (U - J) = 6.0$ eV. We have used the accurate full-potential projector-augmented-wave (PAW) method [20,21] as implemented in the Vienna Ab initio Simulation Package (VASP) [22–24]. The wave functions are expressed in a plane-wave basis set with an energy cutoff of 500 eV, and the self-consistent field energies are converged up to 10^{-6} eV. For our calculations, we used the lattice parameters $a = 4.8928(1)$ Å, $b = 5.5847(1)$ Å, and $c = 5.8251(1)$ Å at 2 K obtained from neutron diffraction refinement. To explore the magnetic ground state, a supercell of size (2 × 2 × 2) with various magnetic configurations of Ni moments is considered. In the present calculations, we used the tetrahedron method with Blöchl corrections for the Brillouin

TABLE I. The effective magnetic couplings and the bond lengths/angles associated with the Ni-O···O-Ni super-superexchange paths of $Li_2Ni(WO_4)_2$ shown in Fig. 2.

$\bar{J}_i$	G-K	2 K				16 K			
	Prediction	Ni-Ni (Å)	O···O (Å)	∠Ni-O···O (deg)	∠O...O-Ni (deg)	Ni-Ni (Å)	O···O (Å)	∠Ni-O···O (deg)	∠O···O-Ni (deg)
$\bar{J}_0$	AF	4.8793(3)	2.635(1)	∠Ni-O1···O3 = 137.429(16)	∠O1···O3-Ni = 89.115(17)	4.8788(2)	2.622(4)	∠Ni-O1···O3 = 137.471(15)	∠O1···O3-Ni = 89.078(17)
$\bar{J}_1$	FM	5.5720(3)	2.932(3)	∠Ni-O3···O2 = 101.604(13)	∠O3···O2-Ni = 164.938(15)	5.5706(2)	2.921(3)	∠Ni-O3···O2 = 101.564(14)	∠O3···O2-Ni = 164.980(12)
$\bar{J}_2$	AF	5.6161(3)	2.796(4)	∠Ni-O1···O2 = 153.990(16)	∠O1···O2-Ni = 114.179(13)	5.6154(1)	2.791(4)	∠Ni-O1···O2 = 153.975(12)	∠O1···O2-Ni = 114.177(16)
$\bar{J}_3$	AF	5.8114(2)	2.833(5)	∠Ni-O3···O2 = 144.561(17)	∠O3···O2-Ni = 126.145(15)	5.8089(2)	2.827(3)	∠Ni-O3···O2 = 144.476(16)	∠O3···O2-Ni = 126.060(16)
$\bar{J}_4$	AF	6.5978(3)	2.450(5)	∠Ni-O3···O3 = 159.644(16)	∠O3···O3-Ni = 159.644(16)	6.5973(2)	2.429(3)	∠Ni-O3···O3 = 159.105(17)	∠O3···O3-Ni = 159.105(17)

TABLE II. Calculated total energy, ΔE (relative to the total energy of the FM state, $E_{\rm FM} = 99.2821$ eV/f.u.), total magnetic moment, $m_s^{\rm tot}$, and atomic moment of Ni, $m_s^{\rm Ni}$.

Config.	ΔE (meV/f.u.)	$m_s^{\rm tot}$ (μ_B/f.u.)	$m_s^{\rm Ni}$ (μ_B/at)
FM	0.0	2.0	1.80
AF1	−3.06	0.0	1.80
AF2	−0.79	0.0	1.80
AF3	−0.93	0.0	1.80
AF4	−3.02	0.0	1.80
AF5	−0.92	0.0	1.80

zone integration with a Γ-centered Monkhorst-Pack k-point mesh of $(9 \times 8 \times 7)$.

Based on the geometric parameters associated with the paths for super-superexchange [16], we have considered five nearest-neighbor spin exchange parameters J_0, J_1, J_2, J_3, and J_4 (see Fig. 2). To extract the values of the spin exchange parameters J_0, J_1, J_2, J_3, and J_4, we expressed the total spin exchange interaction energy of the $Li_2Ni(WO_4)_2$ in terms of the spin Heisenberg Hamiltonian, $H = E_0 + \sum_{\langle ij \rangle} J_{ij} \boldsymbol{\sigma}_i \cdot \boldsymbol{\sigma}_j$. Here J_{ij} is the exchange interaction parameter between the nearest-neighbor Ni site i and site j, and $\boldsymbol{\sigma}_i$ ($\boldsymbol{\sigma}_j$) is the unit vector representing the direction of the local magnetic moment at site i (j). For antiferromagnetic interaction, $J < 0$ is assumed, and for ferromagnetic interaction, $J > 0$ is assumed. The constant E_0 contains all spin-independent interactions. To verify the spin structure determined using neutron diffraction, and under the Goodenough-Kanamori prediction with SSE mechanism modification, as shown in Fig. 6 and Table I, we consider six possible magnetic configurations of the magnetic ground state to evaluate the five spin exchange parameters J_0–J_4, including five AF configurations AF1–AF5 and one FM configuration. The total energies of the supercell of all considered magnetic configurations are given by $E_{\rm FM} = E_0 - 4J_0 - 4J_1 - 4J_2 - 4J_3 - 4J_4$, $E_{\rm AF1} = E_0 + 4J_0 - 4J_1 + 4J_2 + 4J_3 + 4J_4$, $E_{\rm AF2} = E_0 + 4J_0 + 4J_1 - 4J_2 + 4J_3 - 4J_4$, $E_{\rm AF3} = E_0 + 4J_0 - 4J_1 + 4J_2 - 4J_3 - 4J_4$, $E_{\rm AF4} = E_0 + 4J_0 + 4J_1 - 4J_2 - 4J_3 + 4J_4$, and $E_{\rm AF5} = E_0 - 4J_0 + 4J_1 + 4J_2 + 4J_3 - 4J_4$. The relative energies of these configurations calculated using DFT+U are summarized in Table II.

The configuration AF1 has the lowest energy, which is consistent to the experimental findings of a 3D AF spin structure composed of AF coupled FM chains, as shown in Fig. 6. The magnetic moment of Ni is evaluated to be $1.8\mu_B$, which is close to the value of $1.90\mu_B$ fitted from the low-temperature neutron diffraction data. The values of all exchange constants are calculated and listed in Table III.

TABLE III. Calculated nearest-neighbor exchange interaction parameters (in K) along the five directions shown in Fig. 2.

J_0/k_B	J_1/k_B	J_2/k_B	J_3/k_B	J_4/k_B
−4.63	–5.11	–6.12	0.56	–25.32

The antiferromagnetic exchange coupling along the shorter body diagonal direction within the bc plane (J_4/k_B; see Fig. 2) is the strongest (−25.32 K), and is at least four times larger than the rest. This is in excellent agreement with that predicted using the modified Goodenough-Kanamori rule via the SSE path of the shortest O···O distance (Table I). In particular, the broad peak of $\chi(T)$ near ∼19 K (see Fig. 3) that indicates the occurrence of a spin short-range ordering is consistent with the quasi-1D nature implied by the particularly strong J_4 before the 3D AF ground state is achieved.

We also estimated the Curie-Weiss temperature $\theta_{\rm CW}$ [25] in terms of the nearest-neighbor coupling parameters J_0–J_4 for the AF1 spin configuration. In the mean-field approximation, which is valid only in the paramagnetic limit, $\theta_{\rm CW}$ is related to J_i as $\theta_{\rm CW} = \frac{S(S+1)}{3k} \sum_i z_i J_i$, where the summation runs over all the nearest neighbors of a given spin site, z_i is the number of nearest neighbors connected by the spin exchange parameters J_i, and S is the spin quantum number $S = 1$ for Ni. The calculated value of $\theta_{\rm CW}$ using the parameters obtained from GGA+U calculations is −27.07 K, which is in excellent agreement with the experimental value fitted from the magnetic susceptibility data shown in Fig. 3.

F. Negative thermal expansion

We have examined the temperature dependence of lattice parameters for $Li_2Ni(WO_4)_2$ by cooling from room temperature to 2 K, and we plotted the results between 2 and 25 K, in Fig. 7. Interestingly, the negative thermal expansion (NTE) phenomenon is observed below ∼13 K and found to exhibit a minimum near the commensurate antiferromagnetic transition temperature T_{N2}. The lattice parameters along all three axes increase slightly below approximately 13 K, where a, b, and c are increased by approximately 0.02%, 0.04%, and 0.03%, respectively, which corresponds to approximately a 0.1% volume expansion of the unit cell. The net volume coefficient of the thermal expansion α_v of $Li_2Ni(WO_4)_2$ in the temperature range between 2 and 13 K is estimated to be -7.56×10^{-5} K^{-1}, which gives an average linear coefficient of expansion α_l ($= \alpha_v/3$) of -2.52×10^{-5} K^{-1}. The observed volume expansion of $Li_2Ni(WO_4)_2$ below T_{N2} (∼0.1%) is significantly larger than most oxide materials with reported NTE phenomena; for example, such expansions have been found for PrFeAsO and Co_3TeO_6 of 0.015% and 0.067%, respectively [26,27].

The NTE phenomenon occurs below the onset of the AF ordering, which strongly implies the existence of a strong spin-phonon coupling. Although spin-phonon coupling has been found in $CuGeO_3$ and TiOCl to show a dimerized ground state in a 1D spin-Peierls transition of $S = 1/2$, no NTE is expected as a result of translational symmetry breaking from the doubled 1D periodicity, i.e., the periodicity change from a to $2a$ along the chain direction [28,29]. Depending on the chemical compositions, NTE has been explained with various effects including the magnetoelastic volume effect [26], the valence transition [30–32], strong lattice-coupled electronic or magnetic states [33], and structural distortion triggered by excitations of anisotropic lattice vibrations [34–36]. Current substantial NTEs with clear correlation with the onset of an

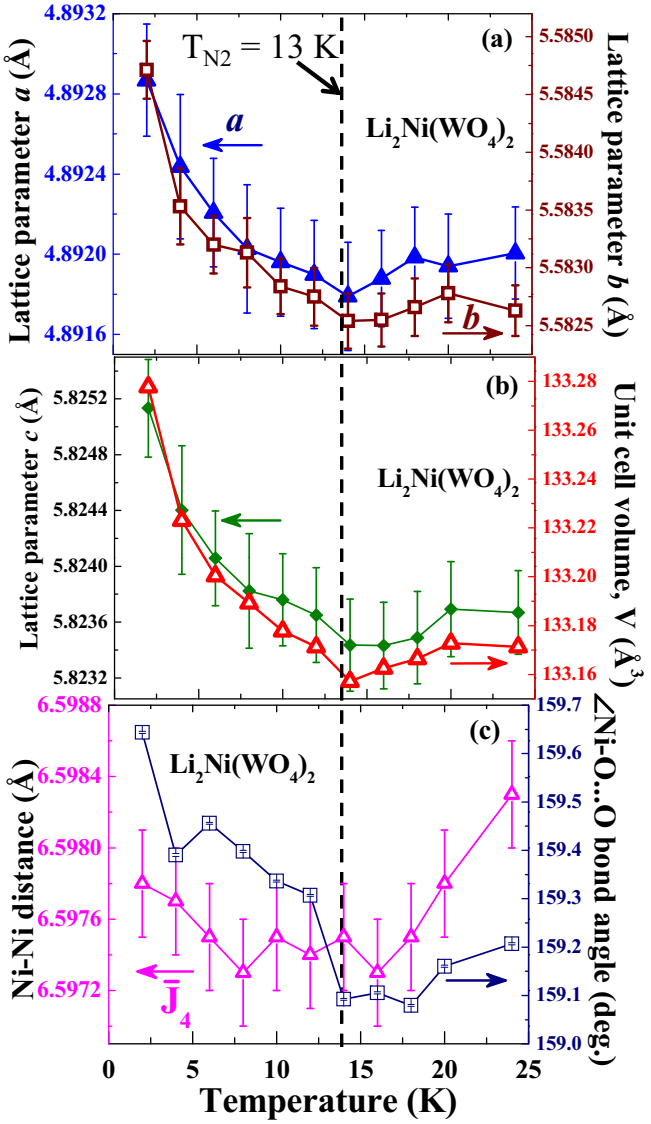

FIG. 7. (Color online) (a) and (b) Temperature dependence of lattice parameters a, b, and c, and cell volume for $Li_2Ni(WO_4)_2$, which all display NTE phenomena below $T_{N2} \sim 13$ K. (c) The thermal variation of the Ni-Ni distance along the $\bar{J}_4$ direction as shown in Fig. 2. The nearly constant Ni-Ni distance and the Ni-O $\cdots$ O bond angle that abruptly approaches $\sim$160° below $T_{N2} \sim 13$ K supports the scenario of competing thermal contraction and long-range spin ordering.

AF long-range spin ordering imply that the strong spin-phonon coupling is responsible for the observed NTE phenomenon.

To understand why and how the NTE phenomenon occurs below $T_{N2} = 13$ K only, bond lengths and bond angles for the double WO_4 and NiO_6 octahedra below T_{N2} and between T_{N1} and T_{N2} are examined. Schematic diagrams of the distorted WO_4 pair and NiO_6 octahedra are illustrated in Fig. 8. Upon cooling from 16 to 2 K in the NTE regime, we observe that the bond lengths of W-O1, W-O2, and W-O5 are increased by 3.92%, 0.83%, and 2.26%; those of W-O3 and W-O4 are reduced by 0.64% and 3.13%, respectively. In addition, the bond lengths of Ni-O1, Ni-O2, and Ni-O5 are reduced by 0.28%, 0.59%, and 0.39%, respectively. However, the bond

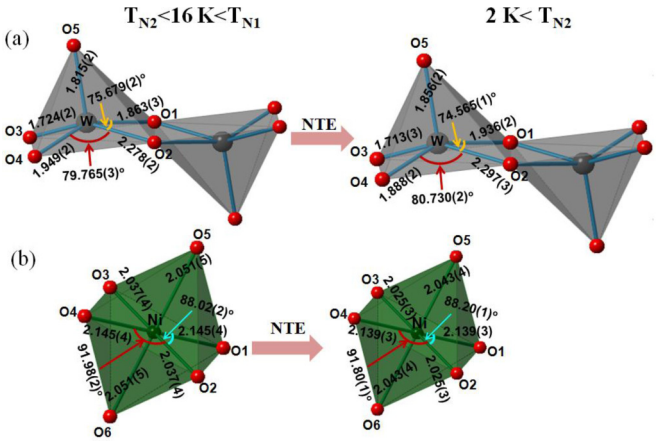

FIG. 8. (Color online) The bond lengths and bond angles at 2 K ($<T_{N2}$) and 16 K (between T_{N1} and T_{N2}) for double WO_4 deformed as an edge-shared inverted square pyramid (WO_5) pair and NiO_6 octahedra.

lengths of Ni-Ni along $\bar{J}_4$ of the strongest AF coupling are found to be nearly constant in the same temperature range [see Fig. 7(c)], which suggests that the Ni-Ni distances are maintained through the relative displacement of oxygens that are corner-shared between double WO_4 and NiO_6 polyhedra, i.e., the expected thermal contraction has been offset by the double WO_4 and NiO_6 local distortion through relative W-O and Ni-O displacement, so that Ni-Ni distances are maintained nearly constant below $T_{N2} \sim 13$ K. In addition, the thermal variation of the Ni-O $\cdots$ O bond angle along the $\bar{J}_4$ direction [defined in Fig. 2(c)] also shows an abrupt increase below T_{N2}, as summarized in Fig. 7(c). The Ni-O $\cdots$ O bond angle below T_{N2} is found to increase approaching $\sim$160°, which agrees with the observation by Whangbo *et al.* that the optimal bond angle for AF coupling via the SSE interaction route is near 160°–165° [37].

Based on the above bond length and bond angle analyses, the reason why the onsets of the NTE phenomena and T_{N2} coincide can be explained reasonably well from the competing regular thermal contraction and the long-range spin ordering. In other words, the regular thermal contraction can push the inter-Ni spin distance closer only when no AF LRO exists. The implication of the current finding is that the AF ordering of SSE type requires an optimal interspin distance and SSE bond angle, and the natural low-temperature lattice contraction must be counterbalanced via local (expansion) distortion through spin-phonon coupling. A similar NTE phenomenon has also been reported in PrFeAsO with a weak correlation between the lattice size and spin ordering, which produced an NTE of only $\sim$0.015% volume increase below $\sim$40 K [26]. However, the onset of NTE was not precisely determined but was well below the antiferromagnetic ordering temperature of $\sim$127 K for the Fe spins. We believe $Li_2Ni(WO_4)_2$ provides the best illustration of spin-phonon coupling-induced NTE phenomena that occur near the onset of AF LRO. In particular, NTE below AF LRO could be a common phenomenon for materials with spin coupling via the SSE route, mainly because of the flexible local distortion of the bridging polyhedra among coupled spins.

IV. CONCLUSIONS

In summary, we have conducted detailed structural and magnetic neutron diffraction studies of $Li_2Ni(WO_4)_2$. The system exhibits a negative thermal-expansion phenomenon that coincides with the onset of the long-range commensurate antiferromagnetic magnetic ordering of Ni spins. An AF ground-state spin configuration is proposed based on neutron diffraction results and confirmed with first-principles density-functional-theory calculations. The reason the NTE phenomenon is associated with magnetic ordering has been explained based on the requirement of optimal interspin distances for the AF long-range ordering through the relative local distortion of double WO_4 that bridges the NiO_6 octahedra.

ACKNOWLEDGMENTS

F.C.C. acknowledges the support provided by the Ministry of Science and Technology (MOST) in Taiwan under Grant No. 103-2119-M-002-020-MY3. G.Y.G. acknowledges the support provided by the Academia Sinica Thematic Research Program and by the MOST in Taiwan under Grant No. 101-2112-M-004-003-MY3. We thank the neutron group of NSRRC for the support under Grant No. MOST 103-2739-M-213-001-MY3. We acknowledge the support of the ANSTO in Australia for providing the neutron beam time that made the neutron diffraction measurements possible.

[1] M. T. Borowiec, V. P. Dyakonov, K. Wozniak, L. Dobrzycki, M. Berkowski, E. E. Zubov, E. Michalski, A. Szewczyk, M. U. Gutowska, T. Zayarnyuk, and H. Szymczak, J. Phys.: Condens. Matter **19**, 056206 (2007).
[2] P. V. Klevtsov and R. F. Klevtsova, J. Struct. Chem. **18**, 339 (1977).
[3] E. V. Zharikov, C. Zaldo, and F. Diaz, MRS Bull. **34**, 271 (2009).
[4] J. Lv, Y. Yuan, X. Huang, H. Shi, H. Tian, Z. Li, T. Yu, J. Ye, and Z. Zou, J. Mater. Res. **23**, 3309 (2008).
[5] M. Alvarez-Vega, J. Rodriguez-Carvajal, J. G. Reyes-Cardenas, A. F. Fuentes, and U. Amador, Chem. Mater. **13**, 3871 (2001).
[6] M. Maczka, J. Hanuza, A. F. Fuentes, and U. Amador, J. Raman Spectrosc. **33**, 56 (2002).
[7] I. P. Muthuselvam, R. Sankar, A. V. Ushakov, G. N. Rao, S. V. Streltsov, and F. C. Chou, Phys. Rev. B **90**, 174430 (2014).
[8] K. M. Ranjith, R. Nath, M. Skoulatos, L. Keller, D. Kasinathan, Y. Skourski, and A. A. Tsirlin, arXiv:1412.5578.
[9] A. W. Sleight, Annu. Rev. Mater. Sci. **28**, 29 (1998).
[10] A. C. Larson and R. B. von Dreele, General Structure Analysis System Report LA-UR-86-748 (Los Alamos National Laboratory, Los Alamos, NM, 2004).
[11] H. M. Rietveld, J. Appl. Crystallogr. **2**, 65 (1969).
[12] P. Kohl and D. Reinen, Z. Anorg. Allg. Chem. **433**, 81 (1977).
[13] J. Rodriguez-Carvajal, Physica B **192**, 55 (1993).
[14] C.-W. Wang, S. K. Karna, R. Sankar, M. Avdeev, I. Panneer Muthuselvam, and F.-C. Chou (unpublished).
[15] J. B. Goodenough, Phys. Rev. **100**, 564 (1955).
[16] J. Kanamori, J. Phys. Chem. Solids **10**, 87 (1959).
[17] H.-J. Koo, D. Dai, and M.-H. Whangbo, Inorg. Chem. **44**, 4359 (2005).
[18] J. P. Perdew, K. Burke, and M. Ernzerhof, Phys. Rev. Lett. **77**, 3865 (1996).
[19] S. L. Dudarev, G. A. Botton, S. Y. Savrasov, C. J. Humphreys, and A. P. Sutton, Phys. Rev. B **57**, 1505 (1998).
[20] P. E. Blochl, Phys. Rev. B **50**, 17953 (1994).
[21] G. Kresse and D. Joubert, Phys. Rev. B **59**, 1758 (1999).
[22] G. Kresse and J. Hafner, Phys. Rev. B **47**, 558 (1993).
[23] G. Kresse and J. Hafner, Phys. Rev. B **49**, 14251 (1994); G. Kresse and J. Furthmuller, J. Comput. Mater. Sci. **6**, 15 (1996).
[24] G. Kresse and J. Furthmuller, Phys. Rev. B **54**, 11169 (1996).
[25] J. S. Smart, *Effective Field Theory of Magnetism* (Saunders, Philadelphia, 1996).
[26] S. A. J. Kimber, D. N. Argyriou, F. Yokaichiya, K. Habicht, S. Gerischer, T. Hansen, T. Chatterji, R. Klingeler, C. Hess, G. Behr, A. Kondrat, and B. Büchner, Phys. Rev. B **78**, 140503(R) (2008).
[27] C.-W. Wang, C.-H. Lee, C.-Y. Li, C.-M. Wu, W.-H. Li, C.-C. Chou, H.-D. Yang, J. W. Lynn, Q. Huang, A. B. Harris, and H. Berger, Phys. Rev. B **88**, 184427 (2013).
[28] M. Braden, B. Hennion, W. Reichardt, G. Dhalenne, and A. Revcolevschi, Phys. Rev. Lett. **80**, 3634 (1998).
[29] M. Shaz, S. van Smaalen, L. Palatinus, M. Hoinkis, M. Klemm, S. Horn, and R. Claessen, Phys. Rev. B **71**, 100405(R) (2005).
[30] J. Arvanitidis, K. Papagelis, S. Margadonna, K. Prassides, and A. N. Fitch, Nature (London) **425**, 599 (2003).
[31] J. R. Salvador, F. Guo, T. Hogan, and M. G. Kanatzidis, Nature (London) **425**, 702 (2003).
[32] Y. W. Long, N. Hayashi, T. Saito, M. Azuma, S. Muranaka, and Y. Shimakawa, Nature (London) **458**, 60 (2009).
[33] K. Takenaka and H. Takagi, Appl. Phys. Lett. **87**, 261902 (2005).
[34] T. A. Mary, J. S. O. Evans, T. Vogt, and A. W. Sleight, Science **272**, 90 (1996).
[35] A. L. Goodwin, M. Calleja, M. J. Conterio, M. T. Dove, J. S. O. Evans, D. A. Keen, L. Peters, and M. G. Tucker, Science **319**, 794 (2008).
[36] J. S. O. Evans, T. A. Mary, T. Vogt, M. A. Subramanian, and A. W. Sleight, Chem. Mater. **8**, 2809 (1996).
[37] M.-H. Whangbo, H.-J. Koo, D. Dai, and D. Jung, Inorg. Chem. **42**, 3898 (2003).